Geophysical Journal International

Geophys. J. Int. (2016) **206,** 1194–1203
Advance Access publication 2016 May 29
GJI Seismology

doi: 10.1093/gji/ggw197

Extracting 220 Hz information from 55 Hz field data by near-field superresolution imaging

Gaurav Dutta,[1] Abdullah AlTheyab,[1] Ahmad Tarhini,[2] Sherif Hanafy[1] and Gerard T. Schuster[1]

[1]*Department of Earth Science and Engineering, King Abdullah University of Science and Technology, Jeddah, Saudi Arabia.*
E-mail: gaurav.dutta@kaust.edu.sa
[2]*Lebanese University, Faculty of Sciences, Lebanon*

Accepted 2016 May 19. Received 2016 May 18; in original form 2016 January 30

SUMMARY

Field experiments are used to unequivocally demonstrate seismic superresolution imaging of subwavelength objects in the near-field region of the source. The field test is for a conventional hammer source striking a metal plate near subwavelength scatterers and the seismic data are recorded by vertical-component geophones in the far-field locations of the sources. Time-reversal mirrors (TRMs) are then used to refocus the scattered energy with subwavelength resolution to the position of the original source. A spatial resolution of $\lambda/10$, where λ is the dominant wavelength associated with the data, is seen in the field tests that exceeds the Abbe resolution limit of $\lambda/2$.

Key words: Controlled source seismology; Wave scattering and diffraction; Wave propagation; Acoustic properties.

1 INTRODUCTION

For a conventional optical lens, the resolution limit for imaging an object is governed by the Rayleigh resolution limit, $\Delta\theta = 1.22\lambda/D$, where θ is the angle between the object and the optical axis of the lens, λ is the wavelength associated with the light and D is the aperture width of the lens (Elmore & Herald 1969; Born & Wolf 1999). The Abbe resolution limit or the diffraction-limited image resolution is restricted to $\lambda/2$ for objects in the near-field of the lens. The finer details of the object less than $\lambda/2$ are permanently lost in the image because of this fundamental diffraction limit. This loss can be attributed to the exponential decay of the energy of the evanescent waves that are emitted from the fine features of the object (Cragg & So 2000; Lerosey *et al.* 2007; Fink 2008; Zhang & Liu 2008).

For subwavelength optical imaging, de Fornel (2001) and Jia *et al.* (2010) utilized this evanescent energy and used it as a basis for their high-resolution optical superlenses. Lerosey *et al.* (2007) demonstrated that superresolution imaging is also possible with microwaves recorded in the far-field region of subwavelength scatterers, as long as the scatterers are within the near-field region of the source. Their microwave experiment with subwavelength scatterers in the near-field of the source showed that imaging resolution could be better than $\lambda/30$ by the use of a time-reversal mirror (TRM) operation (Fink 1993, 2008) applied to the recorded microwave data.

Schuster *et al.* (2012) analysed the TRM operation in the context of seismic scattering and theoretically showed that seismic superresolution is enabled by the contributions from the evanescent field associated with a geometrical-spreading factor. They validated their theory using acoustic and elastic numerical simulations. However, their field data results with the Arizona mine tunnel experiment were not conclusive since they could not verify the presence of subwavelength scatterers in the tunnel walls.

In this paper, we present the first results of a controlled source seismic experiment where we use the TRM operation on seismic data collected in the far-field of the scatterer to accurately image subwavelength scatterers located in the near-field of the source. The precise location of the scatterers is known in our experiment and, hence, we can verify our results with the ground-truth. We also show that, in spite of using seismic data with wavelengths $\geq$5 m, we can resolve finer details of the image with a resolution of 0.6 m.

2 THEORY

Scattered seismic energy from a subwavelength scatterer is very sensitive to the changes in the near-field separation distance r between the source and the scatterer. This strong sensitivity is because the geometrical spreading term $1/r$ is sensitive to small near-field variations in the source-scatterer separation. Here, the near-field region from a subwavelength source can be defined as any location within $\lambda/2$ from the source, whereas the far-field region is any location greater than about $\lambda/2$ from the source. If the receivers are in the far-field region of the source, the recorded seismic energy can be refocused to the source position using a TRM operation (Fink 2008; Schuster *et al.* 2012).

To illustrate this point, Fig. 1(a) shows the rays for a forward scattering experiment, where the strong near-field evanescent

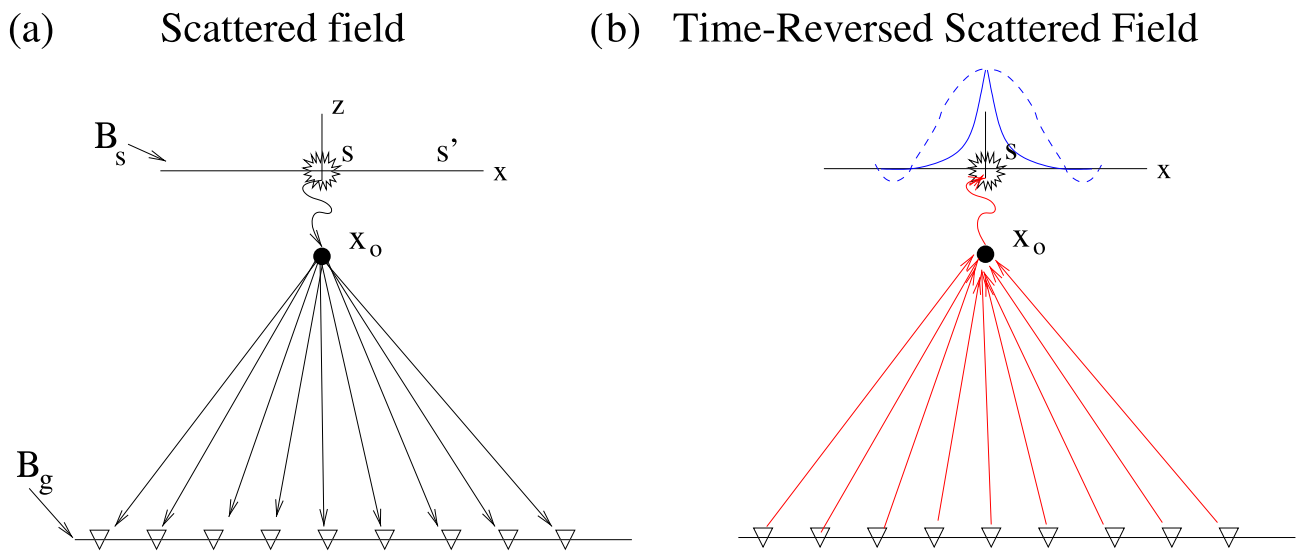

Figure 1. (a) Rays scattering from a subwavelength scatterer at $\mathbf{x}_o$, and the (b) reversed rays associated with the TRM operation. The wiggly ray denotes an evanescent field and the straight rays denote the paths of propagating waves. The solid (dashed) blue curves in panel (b) represent the migration image for a near-field (far-field) scatterer. Here, B_s and B_g represent the source and the geophone lines, respectively, and $\mathbf{s}, \mathbf{s}' \in B_s$.

energy, denoted by the wiggly ray, is converted to a propagating body wave at the scatterer and is transmitted to the far-field receivers. The scattered energy recorded at the geophones $\mathbf{g} = (x_g, y_g) \in B_g$ is denoted as $\Delta D(\mathbf{g}|\mathbf{s})$ in the frequency domain for a source centred at $\mathbf{s} = (x_s, 0) \in B_s$. Here, B_s and B_g represent the source and the geophone lines, respectively.

To image the source location with superresolution, the TRM operation illustrated in Fig. 1(b) reverses the propagation direction of the recorded data at the geophone positions $\mathbf{g} \in B_g$ so that the propagation energy travels backward from B_g to the scatterer at $\mathbf{x}_o$, and then converts to evanescent energy that is focused at the near-field source at the source locations B_s. The focused energy at the trial image point $\mathbf{s}' \in B_s$ for a source at $\mathbf{s}$ is denoted as the migration image $m(\mathbf{s}', \mathbf{s})$ and is computed by the TRM operation (Schuster *et al.* 2012):

$$\mathbf{s}' \in B_s;\ m(\mathbf{s}', \mathbf{s}) = \int_{-\omega_o}^{+\omega_o} \int_{B_g} \overbrace{\Delta D(\mathbf{g}|\mathbf{s})}^{\text{scattered data}}\ \overbrace{G(\mathbf{s}'|\mathbf{g})^*}^{\text{extrapolator}}\, \mathrm{d}x_g \mathrm{d}\omega, \tag{1}$$

where $\omega_o > 0$ is the upper limit of source frequency, $\mathbf{s}'$ and $\mathbf{s}$ are the trial image and source points, respectively, and $G(\mathbf{s}|\mathbf{g})$ is the scattering Green's function in the frequency domain for a point source at $\mathbf{g}$ and geophone at $\mathbf{s}$. The extrapolator $G(\mathbf{s}'|\mathbf{g})$ plays the role of focusing the recorded energy back to the source location. For the TRM operation, the recorded data are used as the extrapolator (Fink 1993, 2008).

In a homogeneous acoustic medium, with velocity c, the Green's function for a point source at $\mathbf{x}'$ and a receiver at $\mathbf{x}$ is given by

$$G(\mathbf{x}|\mathbf{x}') = \frac{\mathrm{e}^{i\omega|\mathbf{x}-\mathbf{x}'|/c}}{|\mathbf{x}-\mathbf{x}'|}. \tag{2}$$

For a bandlimited point source at $\mathbf{s}$ with spectrum $W(\omega)$, the scattered data $\Delta D(\mathbf{g}|\mathbf{s})$ for a point scatterer at $\mathbf{x}_o$, and the extrapolator $G(\mathbf{s}'|\mathbf{g})$ can be represented as

$$\begin{aligned} \Delta D(\mathbf{g}|\mathbf{s}) &= W(\omega) G(\mathbf{g}|\mathbf{x}_o) G(\mathbf{x}_o|\mathbf{s}), \\ G(\mathbf{s}'|\mathbf{g}) &= G(\mathbf{g}|\mathbf{x}_o) G(\mathbf{x}_o|\mathbf{s}'). \end{aligned} \tag{3}$$

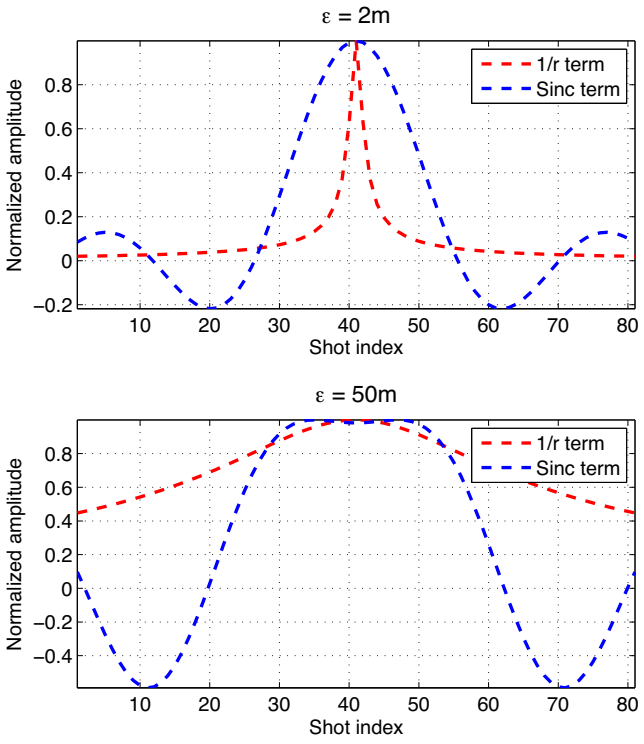

Figure 2. Plots of the sinc-like function and the $1/r$ function for a point scatterer near the shot location 41 at a distance of (a) 2 m, and (b) 50 m from the source. Here, the upper limit of the source frequency is taken to be 1000 Hz and the background velocity as 4000 m s^{-1}. When the scatterer is in the near-field of the source, the lateral resolution is controlled by the geometrical spreading term $1/r$ while for the far-field scatterer, the sinc-like function controls the lateral resolution.

Substituting eqs (2) and (3) into eq. (1) gives

$$\mathbf{s}' \in B_s;\ m(\mathbf{s}', \mathbf{s}) \propto \frac{\mathrm{sinc}(\omega_o[|\mathbf{x}_o - \mathbf{s}| - |\mathbf{x}_o - \mathbf{s}'|]/c)}{|\mathbf{x}_o - \mathbf{s}'|}. \tag{4}$$

Eq. (4) says that the lateral resolution of the TRM image $m(\mathbf{s}', \mathbf{s})$ is controlled by the product of a sinc function and a

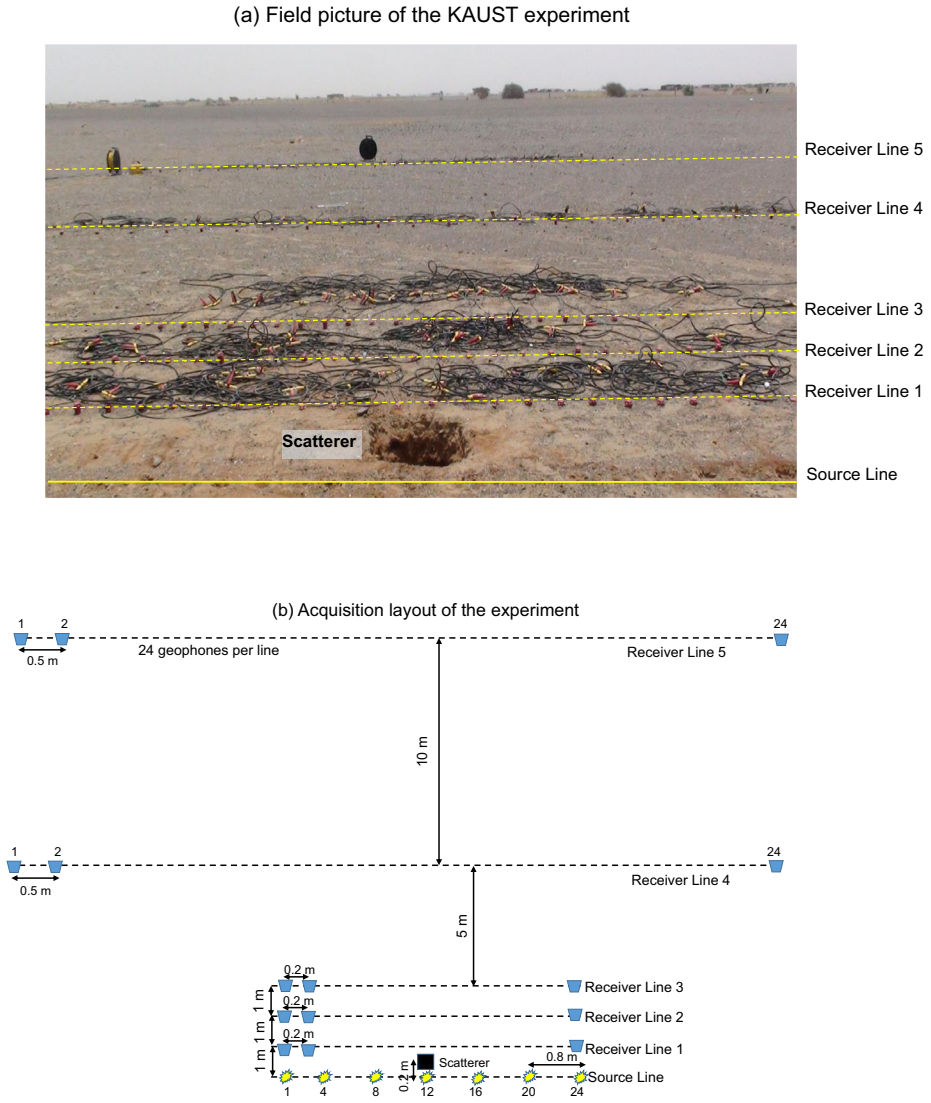

Figure 3. (a) A photo from the KAUST field experiment. The yellow solid line in this figure represents the source line while the yellow dashed lines represent the receiver lines. (b) The acquisition layout of the experiment showing the distance between the sources, the receivers and the scatterer.

geometrical-spreading function $1/|\mathbf{x}_o - \mathbf{s}'|$. The resolution obtained from the sinc function and the geometrical spreading term $1/r$ for different source-scatterer separations can be seen in Fig. 2. If the scatterer is within a distance $\lambda/2$ from the source, then the width of $1/|\mathbf{x}_o - \mathbf{s}'|$ is less than the width of the sinc function's main lobe to enable superresolution imaging. For a near-field scatterer, the migration image $m(\mathbf{s}', \mathbf{s})$ in Fig. 1(b) will look like the blue needle-like curve centred at $\mathbf{s}$, while for a far-field scatterer, the image will be like the dashed sinc-like curve.

Schuster *et al.* (2012) demonstrated the feasibility of TRM superresolution with synthetic seismic data, and their field data experiment was consistent with superresolution imaging. However, it did not unequivocally prove superresolution imaging because there was no control on the insertion or deletion of a subwavelength scatterer in the medium. We now use a controlled field experiment to unequivocally demonstrate, for the first time, the validity of seismic superresolution imaging for a scatterer in the near-field region of the source. The scatterers in our experiments are small holes dug next to the source line. Experimental results are presented for two different sites.

3 FIELD DEMONSTRATION OF SEISMIC SUPERRESOLUTION IMAGING

Two field experiments are used to demonstrate seismic superresolution imaging. In each case, 40 Hz vertical-component geophones are used to record the particle-velocity traces and a 1 kg hammer striking a small metal plate of dimensions $0.1 \times 0.1 \times 0.01$ m^3 is used as the source. The subwavelength scatterers are small holes dug next to the source lines. Multiple receiver lines are used to validate the idea that superresolution imaging is possible even if the recorded data are in the far-field region of the scatterer, as long as the scatterer is in the near-field region of the source.

3.1 KAUST field experiment

The first test is carried out inside the KAUST campus using five parallel receiver lines, each line having 24 geophones with a receiver interval of 0.2 m for the nearest three receiver lines and 0.5 m for the

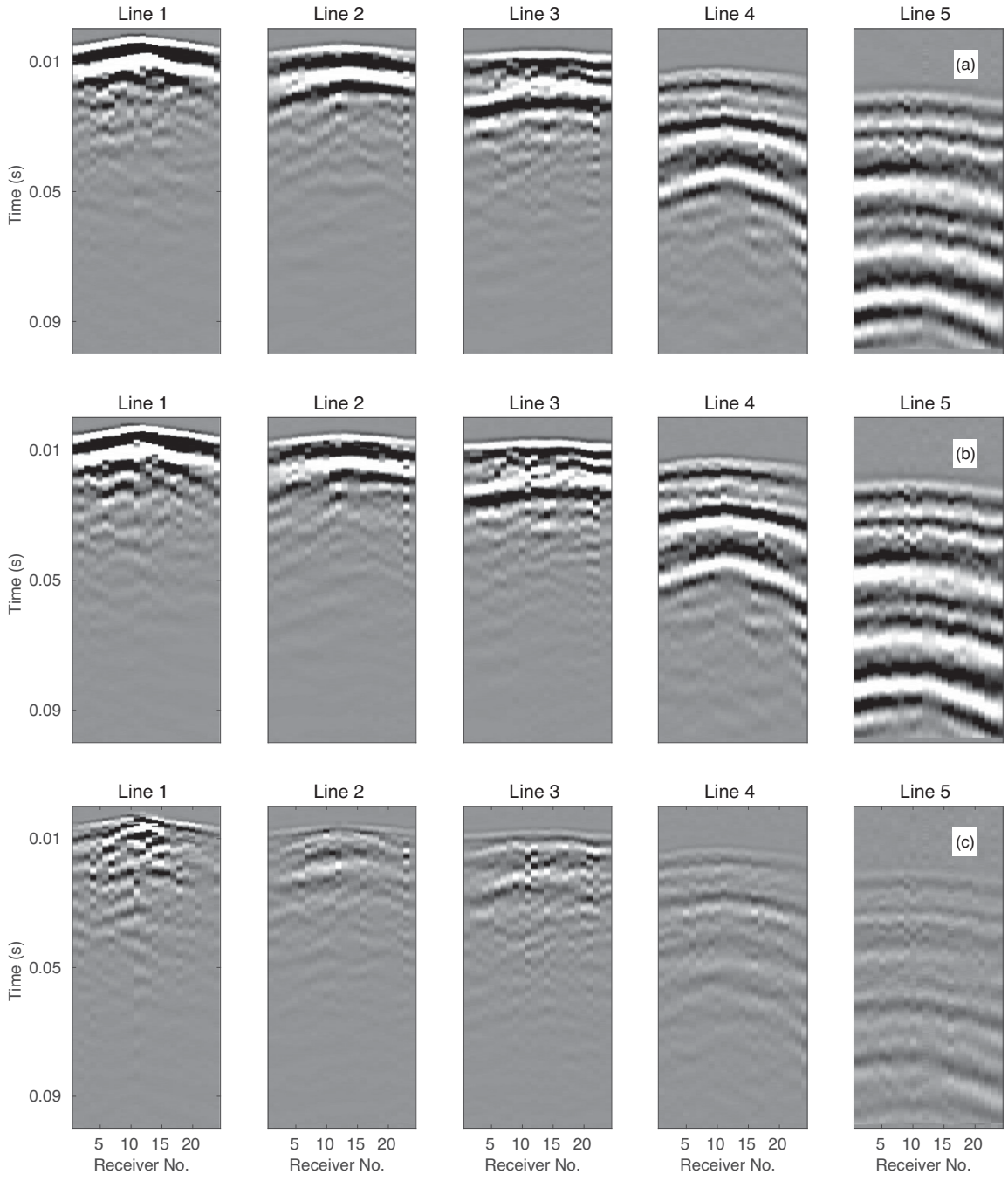

Figure 4. Common shot gathers (CSGs) collected at the shot location 12 (a) before inserting a scatterer and (b) after inserting a scatterer. The shot gathers in panels (a) and (b) are subtracted to get the scattered arrivals in panel (c). For display purposes, a CSG is normalized to its maximum amplitude and then a suitable colour axis limit is selected such that the events in the CSG are clearly visible. The same limit is then used for all the individual subplots in the same vertical panel.

farthest two lines. The five receiver lines are spaced at 1 , 2, 3, 8 and 18 m, respectively, from the source line. There are 24 shots recorded at an interval of 0.2 m on the surface. A field picture showing the experiment set up is shown in Fig. 3(a) while the acquisition layout is shown in Fig. 3(b).

The experiment is conducted in two phases. In the first phase, the data are recorded without the deliberate insertion of a controlled scatterer. This gives the background field $d(\mathbf{g}, t|\mathbf{s}, 0)^{\text{pre}}$ for a source excited at time zero and located at $\mathbf{s} \in B_s$; the recording geophones are at $\mathbf{g} \in B_g$ with the listening time t. In the second phase, traces are recorded after digging a subwavelength hole of dimensions $0.5 \times 0.5 \times 0.5$ m^3 about 20 cm in front of the source line (see the hole in Fig. 3a). The recorded data are denoted as $d(\mathbf{g}, t|\mathbf{s}, 0)^{\text{post}}$ and include the effects of both the background medium and the near-field scatterer. Thus, for each source location, there are two sets of data collected —one having the strong near-field scattered events and one without them. At every shot location, there are 10 stacks collected for both phases. Shot gathers from the two phases of the experiment are shown in Fig. 4.

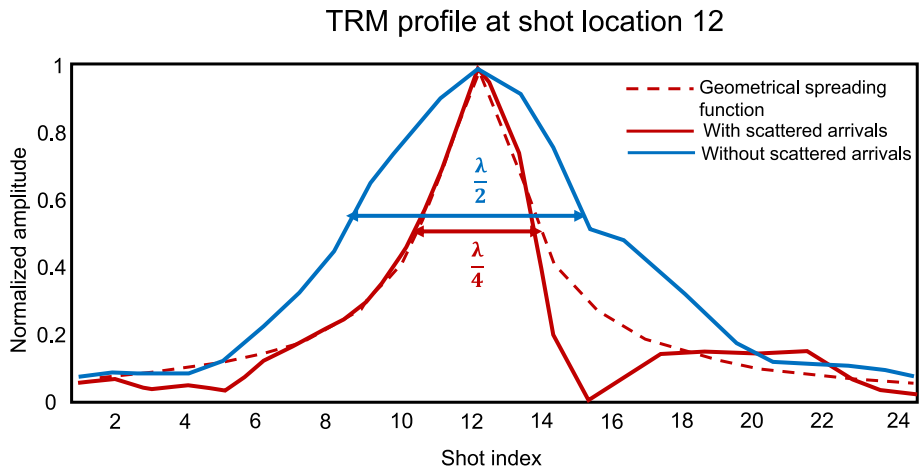

Figure 5. Results from the KAUST field experiment: TRM profile at the scatterer location. The scatterer is located next to the source location 12. The solid blue and red curves show the resolution obtained using the direct and the scattered arrivals, respectively, while the dashed red curve indicates the resolution due to the geometrical spreading function.

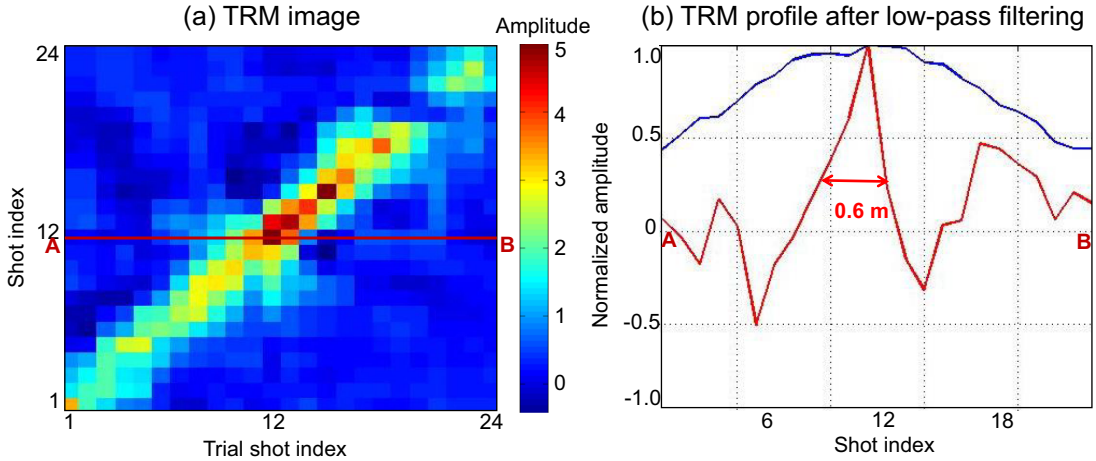

Figure 6. Results from the KAUST field experiment: (a) TRM image for all the trial source locations, and (b) TRM profile in Fig. 5 after low-pass filtering. The solid blue and red curves in panel (b) show the resolution obtained at the source location 25 using the direct and the scattered arrivals, respectively, after the data have been low-pass filtered.

The odd and even numbered shots at each source location are divided to form two shot gather groups (each group having five stacks) at that source location. This is done to avoid false superresolution signatures caused by cross-correlation with random noise. After correcting for some static shifts, they are normalized with respect to the direct-arrival amplitudes to account for source-strength and geophone-response variations and then stacked to give the stacked shot gather $d(\mathbf{g}, t|\mathbf{s}, 0)^{\text{pre}}$. The same procedure is repeated for the data from the second phase of the experiment to give the stacked shot gather $d(\mathbf{g}, t|\mathbf{s}, 0)^{\text{post}}$.

The common shot gathers (CSGs), $d(\mathbf{g}, t|\mathbf{s}, 0)^{\text{pre}}$ and $d(\mathbf{g}, t|\mathbf{s}, 0)^{\text{post}}$, are then subtracted to give the scattered arrivals $\Delta d(\mathbf{g}, t|\mathbf{s}, 0)$ in Fig. 4(c). The scattered data in the frequency domain correspond to $\Delta D(\mathbf{g}|\mathbf{s})$ in eq. (1) and the scattering Green's function $G(\mathbf{s}'|\mathbf{g})$ is approximated by the Fourier transform of $\Delta d(\mathbf{s}', t|\mathbf{g}, 0)$. The direct arrivals are also windowed and the rest of the data are muted. Eq. (1) is then used to compute the TRM images $m(\mathbf{s}', \mathbf{s})$ for $\mathbf{s}, \mathbf{s}' \in B_s$. The migration image $m(\mathbf{s}', \mathbf{s})$ plotted against $\mathbf{s}' \in B_s$ is denoted as the TRM profile for the specified source location $\mathbf{s}$.

Fig. 5 compares the TRM profiles before and after burying the scatterer. The red and blue solid curves in this figure show the resolution obtained from our field experiments with and without using the evanescent energy associated with the scatterer, respectively. The red dashed line indicates the theoretical resolution that should be obtained at the scatterer location, which is proportional to the geometrical spreading factor $1/|\mathbf{x}_o - \mathbf{s}'|$ in eq. (4). It is evident from this figure that the experimental superresolution mostly agrees with the theoretical prediction.

Fig. 6(a) shows the TRM image for all the trial source locations. The hottest colour in this image corresponds to the profile's peak value and occurs at the location of the scatterer. As predicted by the theory in Schuster *et al.* (2012), the peak value is at the source location 12 which is next to the scatterer. The TRM profile for this source location indicates a resolution of $\Delta x = 0.6$ m which is approximately equal to $\lambda_{\min}/4$ and exceeds the Abbe resolution limit of $\lambda_{\min}/2$. In comparison with the source wavelength of 2.5 m, a superresolution signature can be seen due to the near-field scattering from the scatterer.

The maximum frequency and the velocity of the *P*-wave direct arrivals are estimated to be around 110 Hz and 264 m s^{-1}, respectively. Eq. (1) says that the width of the geometrical-spreading function $1/|\mathbf{x}_o - \mathbf{s}'|$, unlike the sinc function, should be independent

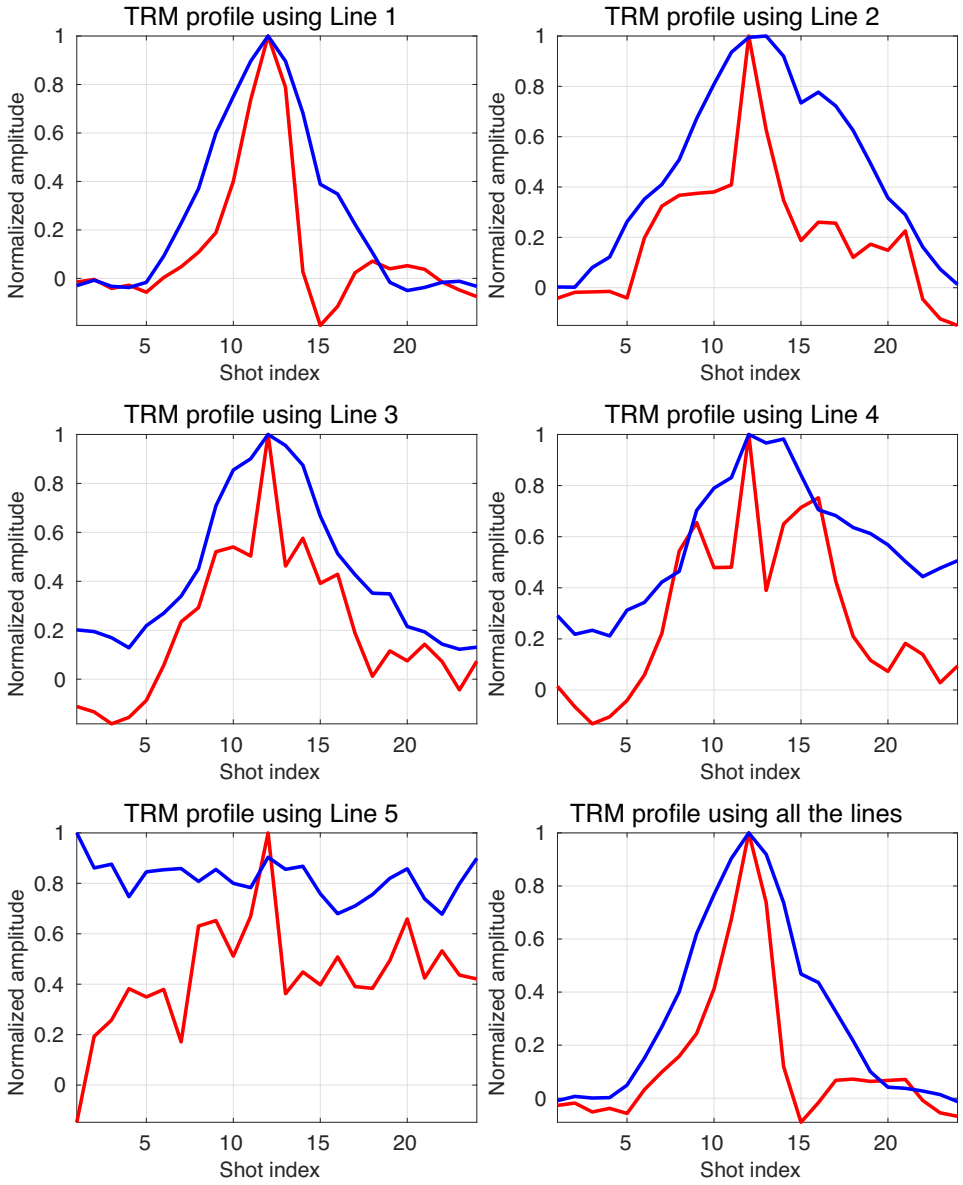

Figure 7. TRM profiles for the individual receiver lines. The solid blue and red curves show the resolution obtained at the source location 12 using the direct and the scattered arrivals, respectively.

of frequency. To test this prediction, a 0–55 Hz low-pass filter is applied to the CSGs. This increases the minimum wavelength of the data, $\lambda_{\min}$, to 5 m. The same TRM operation, as described above, is now applied to the low-pass filtered CSGs. Fig. 6(b) compares the TRM profiles at the scatterer location using the low-pass filtered data. As expected, on reducing the bandwidth of $d(\mathbf{g}, t|\mathbf{s}, 0)^{\text{pre}}$ without the scattered arrivals, the width of the main lobe in $m(\mathbf{s}', \mathbf{s})$ and the wavelength of the data are doubled. However, the resolution obtained from the scattered data $\Delta d(\mathbf{g}, t|\mathbf{s}, 0)$ with the scattered arrivals remains the same ($\Delta x \approx 0.6$ m). In this case, it can also be said that 220 Hz information has been extracted from 55 Hz data with a spatial resolution of $\lambda/8$.

Fig. 7 compares the TRM profiles at the source location 12 using data recorded from the five receiver lines separately. It can be seen from this figure that the resolution of the TRM profile is independent of the receiver-scatterer separation. A resolution of $\Delta x = 0.6$ m is seen for all the individual receiver lines that are in the near-field and in the far-field region of the scatterer.

3.2 Qademah field experiment

To reinforce the findings from the previous experiment, a second seismic experiment is carried out at a test site 40 km north of KAUST. A photo showing the field experiment is shown in Fig. 8(a) while the acquisition geometry is shown in Fig. 8(b). This experiment is carried out in three phases:

(1) The CSGs are recorded on a level ground without any inserted scatterers.

(2) A hole of dimensions $0.9 \times 0.9 \times 0.4$ m^3 is dug into the ground about 20 cm from source location 35 (see the rightmost hole in Fig. 8a). The CSGs are then recorded with the hole now acting as a single near-field scatterer.

(3) Another hole of dimensions $0.9 \times 0.9 \times 0.45$ m^3 is dug near source location 25 (see the leftmost hole in Fig. 8a). This hole is 2.5 m away from the previous scatterer and the CSGs are then recorded with these two near-field scatterers. Both scatterers are 20 cm from the nearest source line.

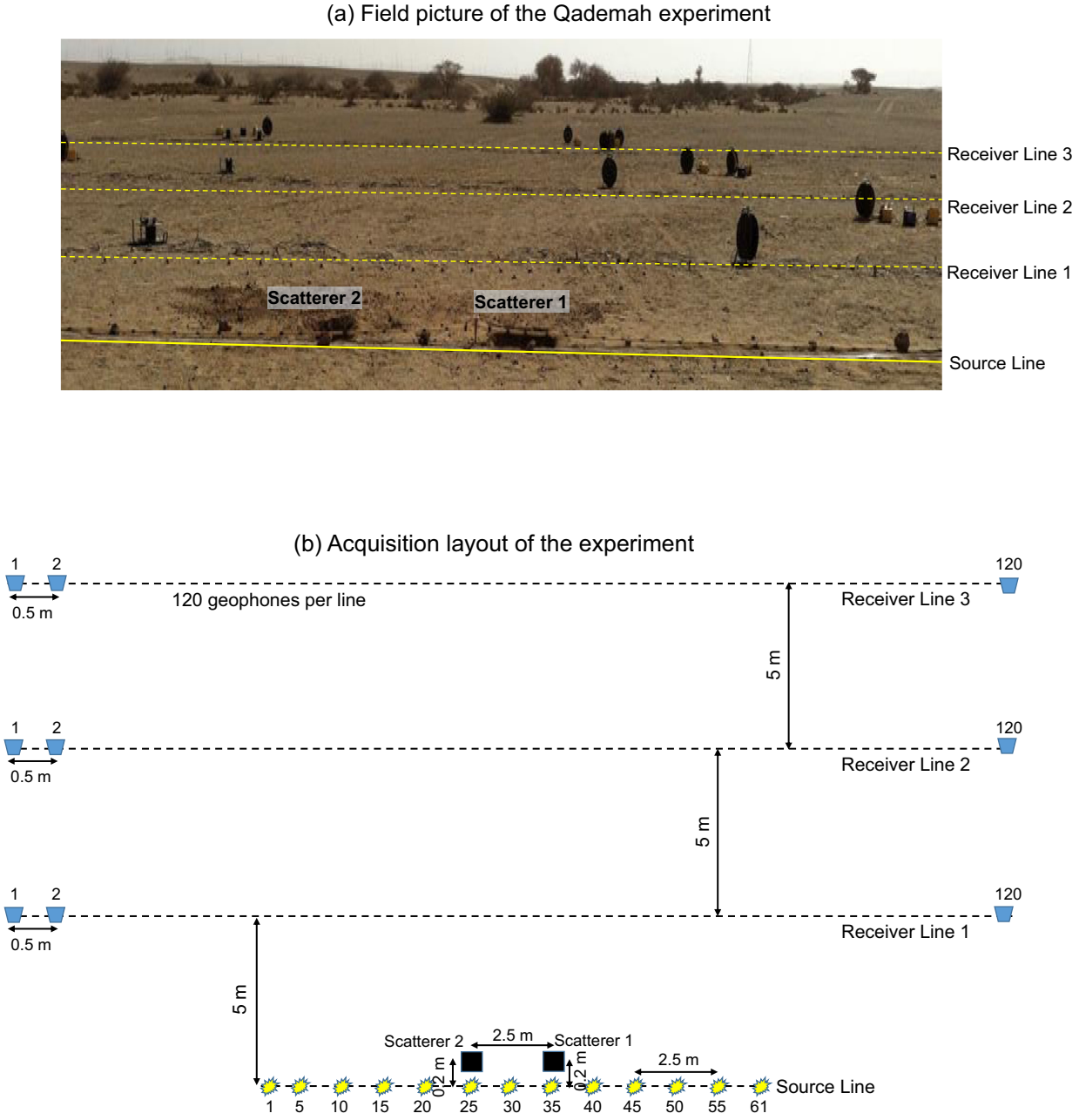

Figure 8. (a) A picture from the Qademah field experiment showing the experiment set up in the field. The yellow solid line in this figure represents the source line while the yellow dashed lines represent the receiver lines. (b) The acquisition layout of the experiment showing the distance between the sources, the receivers and the scatterers.

Sixty-one shots, spaced at 0.25 m, are recorded during each phase of the experiment by three receiver lines, each having 120 geophones with a spacing of 0.5 m between the geophones. The three receiver lines are at a distance of 5, 10 and 15 m from the source line. CSGs from the three phases of the experiments are shown in Fig. 9.

A processing workflow, similar to the one used for the KAUST field experiment, is used to process the data. Fig. 10 shows the TRM profile obtained from the first and second phases of the experiment at the shot location 35. The TRM profile for this source location shows a resolution of $\Delta x = 0.5$ m which is approximately equal to $\lambda_{min}/10$. Also, the theoretical resolution, shown by the dashed red curve in Fig. 10, matches quite well with the experimental resolution obtained (shown by the solid red curve). The same low-pass filter test, as used in the previous section, is used to validate the results. As can be seen from Fig. 11(b), the superresolution signature is preserved because, according to eq. (1), it is independent of the source frequency.

Figs 11(a) and 12 compare the TRM images and the TRM profiles, respectively, using the data from the first and third phases of the experiment. As can be seen from these figures, the scatterer near source location 25 is imaged at its right location with a subwavelength resolution of $\Delta x = 0.5$ m or $\lambda_{min}/10$. As in the previous cases, the resolution is preserved even after the data are low-pass filtered. This can be verified from the TRM profile shown in Fig. 13(b).

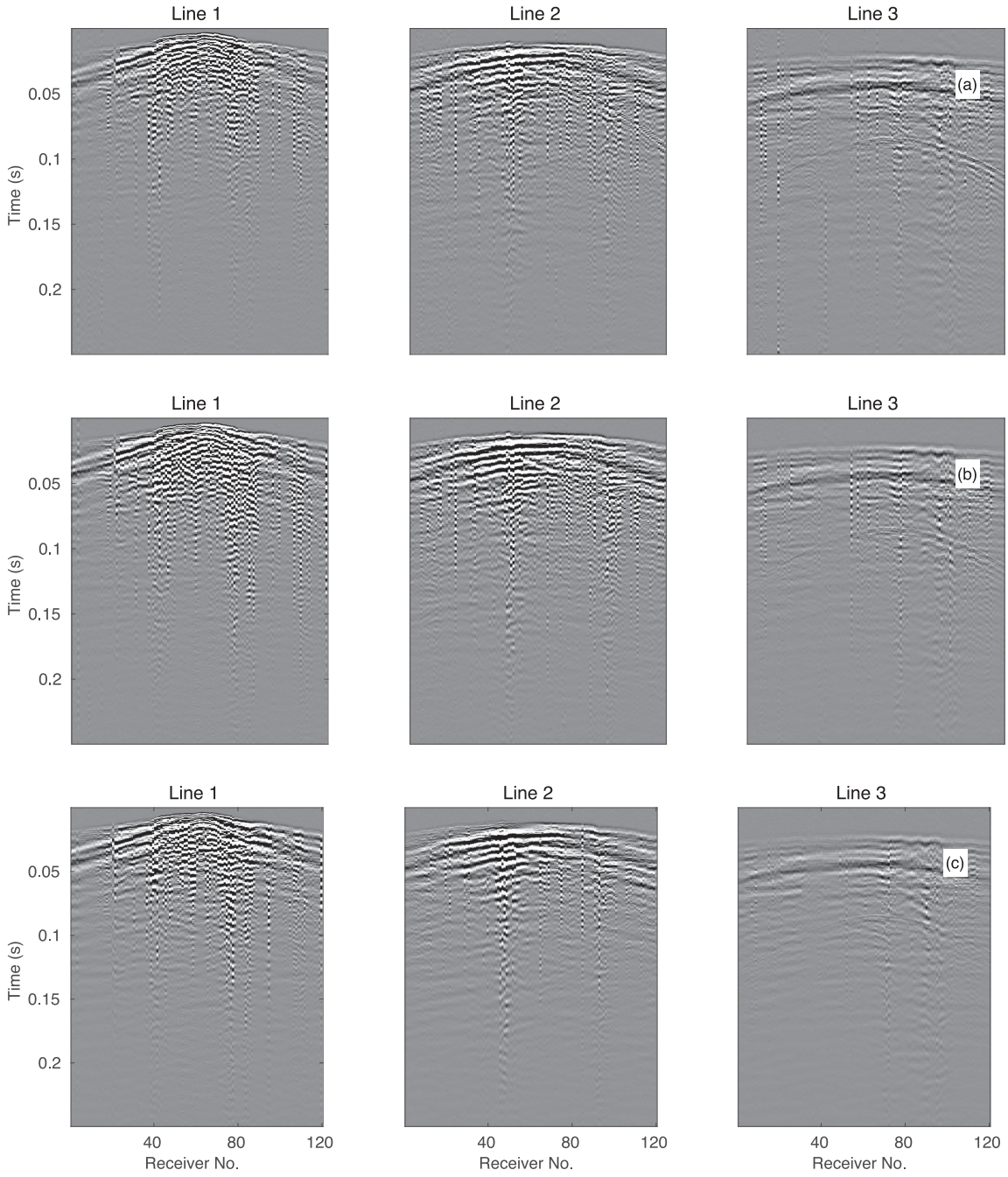

Figure 9. CSGs from the Qademah field experiment at shot location 35 (a) before inserting any scatterer, (b) after inserting a scatterer near shot location 35 and (c) after inserting a scatterer near shot location 25. For display purposes, a CSG is normalized to its maximum amplitude and then a suitable colour axis limit is selected such that the events in the CSG are clearly visible. The same limit is then used for all the individual subplots in the same vertical panel.

4 DISCUSSION

The TRM equations are used to image the near-field scatterers with subwavelength resolution and the superresolution signature is preserved even after a low-pass filter is applied to the recorded data. However, there are some TRM images in Figs 6(a) and 13(a) that show weak superresolution signatures in the absence of a scatterer. For example, the false positive denoted by the arrow in Fig. 13(a). We hypothesize that these false signatures are probably noise in the recorded data getting amplified by the TRM operation in equation 1. These false positives largely disappeared after the low-pass filter operation and the superresolution signature was preserved at only the source location that was close to the scatterer. To obtain reliable TRM images in the presence of noise, it is important to get a sufficient number of stacks at a shot location such that the SNR of the recorded data is at an acceptable level.

The TRM equations do not require the velocity model and the Born approximation is not invoked. It is a form of natural migration (Schuster 2002) that uses the data to form the Green's functions in the migration kernel. This natural migration procedure is now being successfully used to image faults and near-surface heterogeneities from ambient noise data recorded by a dense array of recording stations (AlTheyab *et al.* 2016).

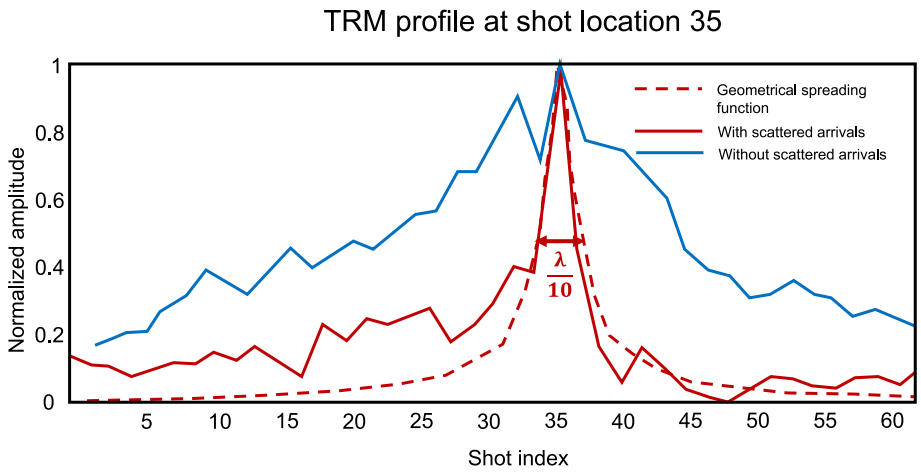

Figure 10. Results from the Qademah field experiment: TRM profile at the scatterer location. The scatterer is located next to the source location 35. The solid blue and red curves show the resolution obtained using the direct and the scattered arrivals, respectively, while the dashed red curve is the resolution due to the geometrical spreading function.

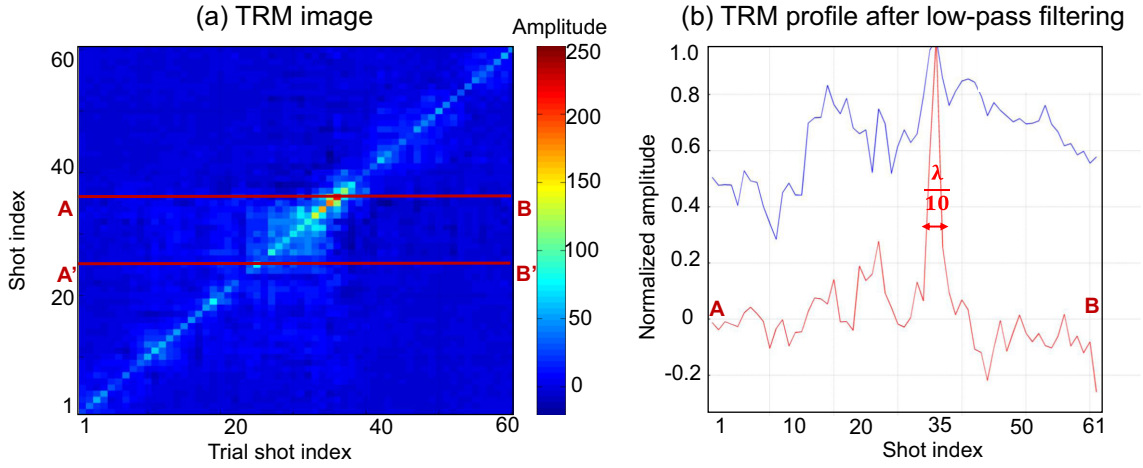

Figure 11. Results from the Qademah field experiment: (a) TRM image for all the trial source locations and (b) TRM profile in Fig. 10 after low-pass filtering. The solid blue and red curves in panel(b) show the resolution obtained at the source location 35 using the direct and the scattered arrivals, respectively, after the data have been low-pass filtered. Here, AB and A′B′ are the TRM profiles taken at the source locations 35 and 25.

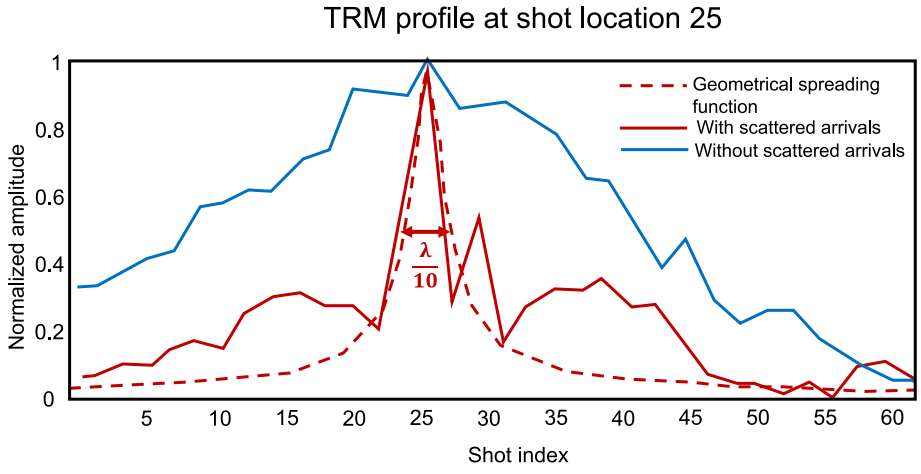

Figure 12. Qademah field experiment results: TRM profile at the scatterer location. The scatterer is located next to the source location 25. The solid blue and red curves show the resolution obtained using the direct and the scattered arrivals, respectively, while the dashed red curve is the resolution due to the geometrical spreading function.

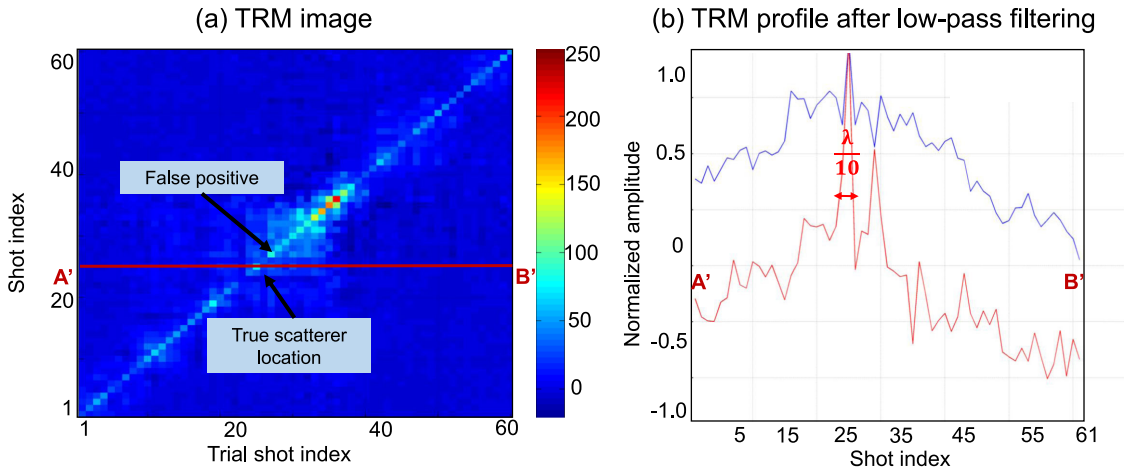

Figure 13. Qademah field experiment results: (a) TRM image for all the trial source locations and (b) TRM profile A′B′ after low-pass filtering. The solid blue and red curves in panel (b) show the resolution obtained at the source location 25 using the direct and the scattered arrivals, respectively, after the data have been low-pass filtered. Here, A′B′ is the profile taken at the source location 25.

5 CONCLUSIONS

Field experiments are used to unequivocally demonstrate seismic superresolution imaging of subwavelength objects using evanescent waves in the near-field of a source. The field tests are for a 1 kg hammer source striking a small metal plate near subwavelength scatterers and the seismic data are recorded by vertical-component geophones in the far-field of the sources. Our results show that seismic resolution of around $\lambda/10$ can be achieved using a TRM operation which exceeds the Abbe resolution limit of $\lambda/2$. In other words, our field experiments prove that it is practically possible to extract 220 Hz information from only 55 Hz data. The superresolution signature is preserved even after the data are low-pass filtered. Superresolution imaging using the TRM operation opens up new avenues for accurate and fast characterization of near-surface faults and sharp lithological boundaries that have important applications in engineering geology and seismic hazard analysis.

ACKNOWLEDGEMENTS

The research reported in this publication was supported by the King Abdullah University of Science and Technology (KAUST) in Thuwal, Saudi Arabia. The authors thank the Editor Dr. Duncan Agnew, Dr. Filippo Broggini and an anonymous reviewer for their comments and suggestions that have significantly improved the paper.

REFERENCES

AlTheyab, A., Lin, F.C. & Schuster, G.T., 2016. Imaging near-surface heterogeneities by natural migration of backscattered surface waves, *Geophys. J. Int.,* **204,** 1332–1341.

Born, M. & Wolf, E., 1999. *Principles of Optics,* Cambridge Univ. Press.

Cragg, G.E. & So, P.T., 2000. Lateral resolution enhancement with standing evanescent waves, *Opt. Lett.,* **25,** 46–48.

de Fornel, F., 2001. *Evanescent Waves: From Newtonian Optics to Atomic Optics,* vol. 73, Springer Science & Business Media.

Elmore, W. & Heald, M., 1969. *Physics of Waves,* McGraw Hill Book Company.

Fink, M., 1993. Time-reversal mirrors, *J. Phys. D: Appl. Phys.,* **26,** 1333, doi:10.1088/0022-3727/26/9/001.

Fink, M., 2008. Time-reversal waves and super resolution, *J. Phys.: Conf. Ser.,* **124,** 012004, doi:10.1088/1742-6596/124/1/012004.

Jia, H., Ke, M., Hao, R., Ye, Y., Liu, F. & Liu, Z., 2010. Subwavelength imaging by a simple planar acoustic superlens, *Appl. Phys. Lett.,* 173507, doi:10.1063/1.3507893.

Lerosey, G., De Rosny, J., Tourin, A. & Fink, M., 2007. Focusing beyond the diffraction limit with far-field time reversal, *Science,* **315,** 1120–1122.

Schuster, G.T., 2002. Reverse-Time Migration = Generalized Diffraction Stack Migration, *SEG Technical Program Expanded Abstracts,* **21,** 1280–1283.

Schuster, G. T., Hanafy, S. & Huang, Y., 2012. Theory and feasibility tests for a seismic scanning tunnelling macroscope, *Geophys. J. Int.,* **190,** 1593–1606.

Zhang, X. & Liu, Z., 2008. Superlenses to overcome the diffraction limit, *Nat. Mater.,* **7,** 435–441.